processes

MDPI

Article

Study on the Prevention and Control of Hydraulic Fracturing Impact Ground Pressure of Hard Roofs During the Initial Mining Period of Thick Coal Seam Fully Mechanized Mining Faces

Jiangwei Liu [1], Kunyu Xing [1], Xuelong Li [1,*], Nan Li [2] and Puci Wang [1]

[1] College of Energy and Mining Engineering, Shandong University of Science and Technology, Qingdao 266590, China; jiangweiliu@cumt.edu.cn (J.L.); 15547905524@163.com (P.W.)
[2] Department of Safety Science and Engineering, Qingdao University of Technology, Qingdao 266520, China; linan@qut.edu.cn
* Correspondence: lixlcumt@126.com

Abstract

To address the rockburst hazard caused by overhanging hard roofs and difficult caving during the initial mining period of thick coal seam fully mechanized working faces, this study takes the N4202 fully mechanized top coal caving working face of the Santunzi Coal Mine as the field engineering background. The mined No. 4-1 coal seam has an average thickness of 9.46 m, and its overlying hard roof is composed of medium sandstone and siltstone. A total of 39 hydraulic fracturing boreholes, including type A, type B, type C1/C2, and fan-shaped holes, were deployed, with a designed fracturing depth of 19 m. Three testing means, including a CXK12(B) borehole imaging instrument, a KJ1222 microseismic monitoring system, and on-site roof caving observations, were adopted to comprehensively evaluate the field performance of roof hydraulic fracturing, and the rockburst prevention mechanism was analyzed. The field test results indicate that dense and well-connected fractures are formed after fracturing, with more than 8 fractures per single borehole and a fracture aperture of 0.8–2.2 mm, and the connectivity rate between adjacent fracturing boreholes reaches 92.3%. The initial mining top caving step distance of the working face is reduced to 13.2 m, while the theoretical calculated values are 10 m for the immediate roof and 15.6 m for the main roof. The roof gradually collapses, and the mining pressure is alleviated. During fracturing, the frequency and energy of microseismic events increase by 285% and 230%, respectively, compared to the state before fracturing. In the subsequent mining process, the maximum microseismic energy is only 4.56 kJ, which is far lower than the rockburst critical energy threshold (20 kJ) of this mine. Therefore, no rockburst hazard occurs in the working face. These research findings can provide a practical technical reference for rockburst prevention using hard roof hydraulic fracturing in similar thick coal seam fully mechanized mining faces.

Keywords: thick coal seam; hard roof; impact ground pressure; initial mining; caving

Check for updates

Received: 30 May 2026
Revised: 21 June 2026
Accepted: 22 June 2026
Published: 29 June 2026

Copyright: © 2026 by the authors. Licensee MDPI, Basel, Switzerland. This article is an open access article distributed under the terms and conditions of the Creative Commons Attribution (CC BY) license.

1. Introduction

As the depth of coal mining continues to increase and the intensity of mining continues to improve, the geological hazards faced during the process of fully mechanized mining of thick coal seams are becoming increasingly prominent [1–5]. Among them, rockburst, as a highly sudden, destructive, and complex coal mine dynamic disaster, has become a key bottleneck restricting the safe and efficient mining of thick coal seams [6–10]. Rockburst is

a dynamic phenomenon in which the accumulated elastic potential energy in underground rock masses is suddenly released, leading to severe rock fragmentation, tunnel deformation, equipment damage, and even casualties [11,12]. According to statistics, rockburst accidents caused by the suspension of hard roof panels in thick coal seam fully mechanized mining faces in China account for more than 60% of total rockburst accidents, causing huge economic losses and casualties [13]. Conducting research on the prevention and control of rockburst in hard roof panels has important practical significance and engineering value [14–18].

Fully mechanized top coal caving, with its advantages of high mining efficiency, high resource recovery rate, and low production cost, has become the mainstream technology for thick coal seam mining and is widely used in major coal mines in China. However, in the application of this technology, some working face roof rock layers have the characteristics of high strength, good integrity, and dense cementation, forming a hard roof. Such roofs are difficult to cave during mining and are prone to forming large areas of suspended roof [19]. Under the pressure of the overlying rock, the suspended roof will accumulate a large amount of elastic potential energy [20]. When the potential energy reaches its limit, sudden fracture and collapse occur, generating strong impact dynamic pressure, which triggers impact ground pressure disasters and seriously threatens the operational safety of the working face.

At present, the technologies for preventing and controlling the impact ground pressure of hard roofs at home and abroad mainly include roof blast pre-cracking, hydraulic fracturing, water injection for roof softening, forced roof caving, pressure-relief drilling, etc. [21]. Among them, roof blast pre-splitting is simple to execute and cost-effective, but the blasting vibration is large, the pre-splitting effect is uneven, and it causes significant disturbance to the surrounding rock [22], which can easily trigger secondary disasters [23]. Water injection for roof softening is only suitable for rock formations that are easily softened by water and has poor effects on hard sandstone and other rock formations [24]. Forced roof caving requires a large amount of manpower and material resources [25], and the roof caving effect is difficult to control [26]. By contrast, hydraulic fracturing has been widely applied and the technology has been rapidly developed for the treatment of hard roofs due to its advantages of operational safety [27–29], minimal disturbance to the surrounding rock, uniform pre-fracturing effect, controllable cost, and easy operation [30]. This technology injects high-pressure water into the borehole, using water pressure to create cracks in the roof rock layer and expand them, forming a network of interconnected cracks. This weakens the mechanical strength of the roof, damaging its integrity, which promotes timely and stable collapse of the roof and avoids the accumulation of energy in the suspended roof that may cause impact ground pressure [31,32].

In recent years, scholars both domestically and internationally have conducted extensive research on the hydraulic fracture propagation mechanism and anti-rockburst parameter optimization of hard roof hydraulic fracturing, forming a relatively complete theoretical and technical system. Kang et al., based on field experiments and numerical simulations, found that hydraulic fracturing can reduce the overall lateral support pressure of the working face. They proposed that the hydraulic fractures and primary fractures formed by hydraulic fracturing and their shear slip are the fundamental reasons for pressure relief [33]. Chang et al. found that hydraulic fracturing for roof caving reduced the deformation and failure of the surrounding rock in the roadway and improved the integrity of the surrounding rock [34]. Liu et al. explored the application of hydraulic fracturing in the prevention and control of hard roof impact ground pressure [35], taking into account the geological conditions of thick coal seams in China [36]. However, due to significant differences in geological conditions among different coal mines [37], the lithology, thick-

ness, and mechanical properties of roof rock layers vary [38]. The parameter design and execution of hydraulic fracturing need to be optimized according to specific working face conditions, and existing technical solutions cannot be blindly applied [39].

Although previous studies have verified the effectiveness of hydraulic fracturing for hard roof rockburst control, there are still obvious deficiencies when targeting thick coal seam fully mechanized mining faces. First of all, most existing studies focus on conventional thin coal seams or single-type fracturing borehole layout, while systematic research on layouts with multiple types of fracturing boreholes (such as parallel holes, fan-shaped holes, and end-protection holes) for large-thickness coal seams is insufficient, lacking targeted layout schemes adapted to the spatial characteristics of thick coal face roadways and cutting holes. Second, most existing construction parameter studies only adopt empirical values or single-factor analysis and rarely integrate mechanical models of fixed-end roof beams, physical and mechanical parameters of the rock layer, and actual working conditions to carry out quantitative calculation and multi-index optimization of fracturing pressure, fracturing time, and borehole spacing. In addition, few studies have specifically optimized multi-stage hydraulic fracturing for the initial mining stage of thick coal seams, ignoring the particularity of overhanging-roof risk during initial mining. Aiming to address the abovementioned research gaps, this study carries out targeted research on borehole layout and parameter optimization for the N4202 thick coal seam working face, which overcomes the deficiencies of existing research and provides strong engineering and innovative value.

The N4202 fully mechanized mining face, as the first working face in the N42 panel area, is a thick coal seam where the No. 4-1 coal seam is being mined. The roof is mainly composed of medium sandstone and siltstone, and the rock layers are hard and intact. During the initial mining period, the face is prone to forming an overhanging roof, which poses a serious risk of rockburst [40]. To ensure safe and efficient mining of the working face, it is imperative to carry out research on the prevention and control of rockburst under the hard roof during hydraulic fracturing [41]. In this work, taking the N4202 working face as the engineering background, the working face conditions [41], hydraulic fracturing mechanism, on-site application, and effect evaluation are systematically studied, aiming to solve the problem of preventing and controlling hard top plate impact ground pressure in this working face [42]. At the same time, it provides a technical reference for the prevention and control of the impact ground pressure of hard top plates in similar thick coal seam fully mechanized mining faces in China, promoting the safe development of thick coal seam fully mechanized mining technology [43,44].

2. Working Face Conditions

2.1. Geological Conditions of the Working Face

The N4202 fully mechanized mining face is the first mining face in the N42 mining area. It adopts a long wall and parallel coal roadway layout, with a dip length of 257.5 m and a strike length of 1368 m (the actual excavation strike length is 1497 m, the inclined length is 257 m, and the working face area is 384,729 m^2). As shown in Figure 1, the working face is excavated along the coal seam floor with a rectangular cross-section, with a width of 10.0 m and a height of 3.6 m. It is connected to the return air channel to the north, the belt channel to the south, the direction of the old pond to the west, and the direction of the working face to the east. The installation of the comprehensive mining equipment has been completed. The working face is mining coal seam No. 4-1, with a total thickness of 6.58–12.34 m, an average thickness of 9.46 m, and an inclination angle of 4–8°, with an average of 6°. The coal seam runs northeast to southwest and leans southwest, appearing as black blocks with light, brownish black stripes and uneven fracture surfaces. It has a

weak asphalt luster and is mainly composed of dull coal, followed by bright coal. It belongs to the semi-dull primary structure coal.

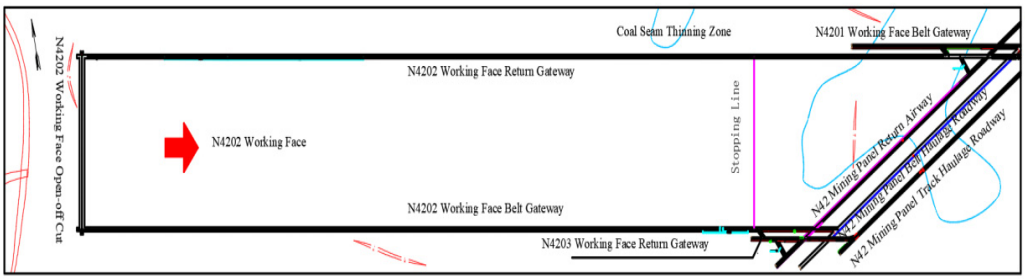


Figure 1. Mining map of N4202 working face.

There are no buildings, rivers, or lakes on the surface of the working face. The terrain is high in the north, low in the south, high in the east, and low in the west. The highest point in the north is 1103 m, and the lowest point in the south is 1045 m, with a height difference of 58 m between north and south. The surface vegetation is sparse, with a ground elevation of 1025–1045 m and a working face elevation of 730–780 m, with a burial depth of 320–403 m. The underground position is located north of the N42 mining area, with the N4201 working face in the north, the N42 return airway in the east, and the N4203 working face in the south, and 70 m from the boundary of the N42 mining area in the west. The specifications of the working face roadway are: belt groove 5.4 × 3.6 m, return airway 4.7 × 3.6 m, and cut hole 10.0, as shown in Table 1.

Table 1. Detailed parameters of working face position and surrounding relationship.

Project Category	Specific Project	Parameter
Basic Overview	Coal seam name	4-1 coal seam
	Horizontal name	+750 m
	Mining area name	N42 panel area
	Working face name	N4202 Fully mechanized top coal caving working face
	Ground elevation	1025~1045 m
	Working face elevation	730~780 m
	Buried at a depth	320~403 m
Tunnel parameters	Tape groove specification	5.4 × 3.6 m
	Return air duct specification	4.7 × 3.6 m
Coal seam parameters	The total thickness of the coal seam	6.58~12.34 m (average 9.46 m)
	Coal seam dip angle	4~8° (average 6°)
	Coal body structure	Primary structure coal

The top and bottom plates of the working face are composed of hard rock layers, among which the old roof is composed of medium sandstone, which has strong integrity, is difficult to collapse, and is the main control object of rockburst. The specific lithology, thickness, and physical and mechanical parameters of the top and bottom plates are shown in Table 2.

Table 2. Specific lithology, thickness, and physical and mechanical parameters of the top and bottom plates.

Top and Bottom Plate Name	Rock Name	Thickness (m)	Lithological Characteristics	Compressive Strength (MPa)	Tensile Strength (MPa)	Other Parameters
Old top	Medium sandstone	5.9~12.7	Light gray, thick layered structure, medium sand structure, calcium cementation, poor sorting, thin layers of interbedded sandstone	12.8~37.2	1.09~3.5	Softening coefficient: 0.35~0.52
Direct top	Siltstone	1.8~5.5	Light gray, thick layered structure, silty structure, interbedded with thin layers of medium sandstone	2.7~25.6	0.4~2.8	Nothing
Pseudo top	Carbonaceous mudstone	0.2~0.4	Black, medium thick layered, lightweight, uneven fracture surface, fragmented rock core, easily weathered and broken	1.2~18.6	0.2~2.1	Nothing
Direct Bottom	Fine sandstone	0.3~0.8	Dark gray black to dark gray, fine sandy structure, calcareous cementation, bottom medium thick layer fine gravel structure, thick layered	2.82~59.9	0.15~4.58	Nothing
Old base	Coarse sandstone	3.5~3.7	Gray-white, blocky structure, dense calcareous cementation, mainly composed of quartz and feldspar	13.6~39.7	2.1~3.8	Nothing

2.2. Cutting Eye Support Conditions

The N4202 working face adopts a combined support method consisting of anchor rods, anchor cables, W-steel strips, steel bars, support beams, and mesh for the cutting hole. The specific support parameters are as follows, and the cutting hole section and support are shown in Figure 2.

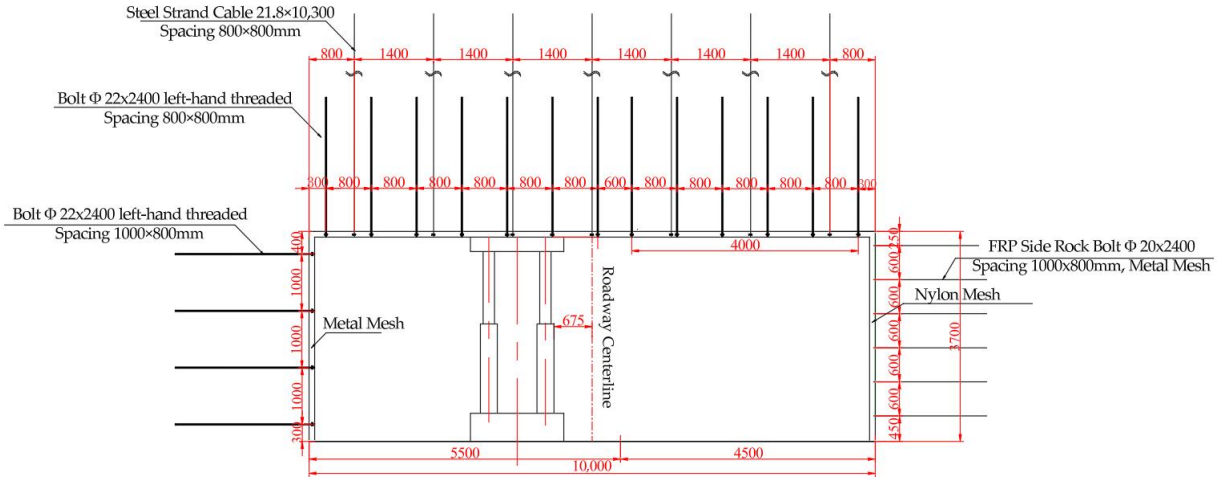


Figure 2. Cutting section and support of N4202 working face.

2.2.1. Roof Support

Roof anchor cable: SKP22/1×19S/1860 mining anchor cables are used, with a length of 8300 mm and a spacing of 1400 × 900 mm between rows. Three cables are arranged in each row, and four cables are arranged in each row at the installation location of the coal mining machine. The accessories are made of 300 × 300 × 16 mm high-strength arched trays, matched with high-strength adjustable center ball pads and locks. Three MSK2360 resin anchoring agents are used for anchoring, with a pre-tightening force of not less than 300 kN.

Roof anchor bolts: MSGLW-500/22 × 2800 mm anchor bolts are used, with a spacing of 800 × 900 mm between rows, and 6 bolts are arranged in each row. Seven bolts are arranged in each row at the installation site of the coal mining machine. Using high-strength anchor bolts and nuts, combined with high-strength arch trays, self-aligning ball pads, and nylon washers, the top and upper anchor bolts are both made of 150 × 150 × 10 mm high-strength arch trays. The top anchor bolt is anchored with two MSK2360 resin anchoring agents, with an anchoring force of not less than 190 KN and a pre-tightening force of 400 N·m.

2.2.2. Assistance and Support

The mining support anchor rods are MGSL-22/2400F φ 22 × 2400 mm fully threaded resin anchor rods, with a spacing of 600 × 900 mm and 6 rods per row. The fiberglass anchor rods are circular plastic trays with a diameter of φ 120 mm, anchored using one MSCKb2335 and one MSK2360 resin anchor agent, with a pre-tension force of not less than 70 N·m.

2.2.3. Mesh

The roof is supported by a warp and weft mesh made of a single 10# iron wire, with a mesh size of 50 × 50 mm and dimensions of 4700 × 1000 mm. The mining support mesh is made of nylon mesh. The mesh adopts long-edge docking, and the short edge overlap is not less than 100 mm. It is connected with 16# iron wire, a double wire double buckle, a hole connection, twisted for not less than 3 turns, and the iron wire is combed into braids.

The metal mesh is laid flat, closely attached to the wall, firmly connected, and without mesh pockets.

2.2.4. W Steel Strip and Steel Bar Support Beam

The roof anchor rod is supported by a W-steel strip with a specification of 4300 × 250 × 5 mm; the roof anchor cable is supported by a steel bar support beam made of 16# round steel, featuring a 3400 × 80 mm welded double-bar double beam.

2.3. Mechanism of Hydraulic Fracturing and Anti-Collision of Roof During Initial Mining Period

During the initial mining process of the coal mining face, the roof of the goaf experiences an O-X type fracture. As the face advances, the middle of the roof undergoes periodic fracture, and the end part is supported by the coal pillar, forming a triangular overhanging roof. The end of the triangular roof also undergoes periodic fracture as the face advances. When the roof above the working face is relatively hard, the roof collapse section and the triangular area at the end are difficult to collapse during the initial mining period, and a hanging roof easily forms. From the perspective of mechanical mechanism analysis, the suspended roof in the initial and end mining stages behave as fixed-end support beam structures. During the initial mining period, the hard roof overhangs the coal body on the working face side and the cutting eye side, which can be regarded as two fixed-end support beams. As the working face advances, the overhanging distance of the hard roof increases. Under the pressure of the overlying rock, when it reaches its ultimate span, the first fracture and collapse occur. Therefore, the control strategy is to artificially increase the number of cracks in the hard roof through hydraulic fracturing at the cutting hole, forming a complex network of hydraulic fractures that destroys its integrity. This changes the constraint conditions and fracture characteristics of the roof at the support point, promoting timely collapse of the goaf overhanging roof and achieving the goal of preventing stress accumulation, improving the stress environment, and reducing impact risk. The principle of hydraulic fracturing for initial mining top caving is shown in Figure 3.

According to the principle that the height of the roof collapse after cracking should fill the goaf, combined with the mining height M = 12.46 m and the fragmentation coefficient K_p = 1.3, the fracturing height is calculated using the following formula:

$$\sum h = \frac{M}{Kp - 1} \quad (1)$$

Substituting the parameters into the formula yields: $\sum h = \frac{12.46}{1.3-1} = 41.5$ m.

This theoretical formula is derived based on the ideal working conditions that all overlying strata fully collapse and fill the entire goaf. However, based on field geological surveys, rockburst risk assessment, and economic evaluations, the overlying strata contain abundant low-strength mudstone and sandy mudstone, which can collapse spontaneously if mined without artificial fracturing. Only the medium sandstone and siltstone strata that are closely related to rockburst hazard are selected as the target fracturing layers. Therefore, the actual construction fracturing height is set to 19 m rather than the theoretical 41.5 m.

As shown in Figure 4, the drilling distance of sand supplement 3-1 in the N4202 working face is 440 m from the cutting hole. Based on the column chart of the drilling hole, a comprehensive analysis of the lithology and overlying rock factors affecting the stress environment and impact risk of the working face is conducted to determine the key fracturing zones within the direct roof and old roof. The final fracturing height is determined to be 19 m, involving the following lithologies: 1.24 m sandy mudstone, 0.6 m sandy mudstone, 0.5 m mudstone, 0.95 m sandy mudstone, 0.9 m sandy mudstone, 8.82 m mudstone, 3.4 m fine-grained sandstone, 2.06 m sandy mudstone, and 4.26 m siltstone.

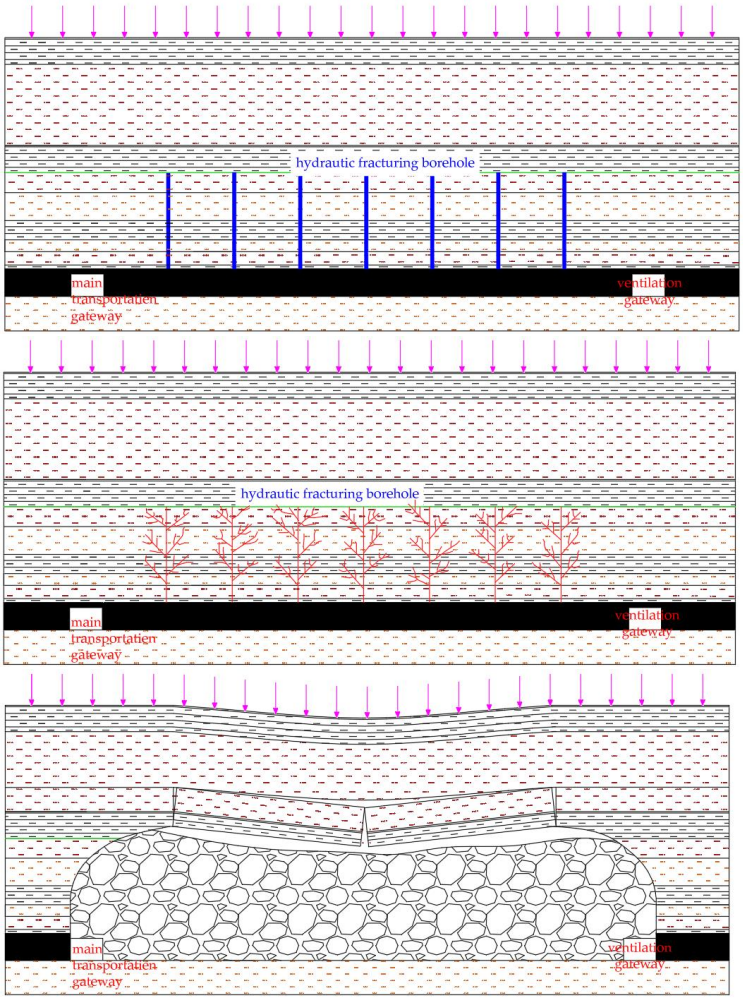


Figure 3. The principle of hydraulic fracturing and initial mining top caving in N4202.

Lithology	columnar	thickness	Lithological description
Mudstone		3.73	Light gray, with slip surfaces, horizontal bedding, RQD=10%.
Fine-grained sandstone		0.60	Light gray, composed mainly of quartz and feldspar, RQD=75%.
Siltstone		5.00	Light gray, calcareous cementation, core short columnar, RQD=40%.
Coal		0.50	Black, brown streak, weak luster, conchoidal fracture, massive structure.
Fine-grained sandstone		0.90	Dark gray, with slip surfaces, horizontal bedding, core short columnar, RQD=60%.
Sandy mudstone		3.60	Light gray, calcareous cementation, containing coal debris and plant fossils, core short columnar, RQD=40%.
Coal		0.60	Brown streak, weak luster, conchoidal fracture, massive structure.
Sandy mudstone		8.82	Light gray, with slip surfaces, horizontal bedding, core short columnar, RQD=30%.
Siltstone		4.26	Light gray, calcareous cementation, horizontal bedding, core short columnar, RQD=40%.
Sandy mudstone		2.06	Light gray, with slip surfaces, conchoidal fracture, RQD=10%.
Fine-grained sandstone		3.40	Light gray, composed mainly of quartz and feldspar, medium sorting, RQD=60%.
Mudstone		8.82	Light gray, interbedded with medium-thick sandy mudstone and thin carbonaceous mudstone, RQD=30%.
Sandy mudstone		0.90	Light gray, with slip surfaces, conchoidal fracture, RQD=55%.
Coal		0.50	Black, brownish-black streak, dominated by bright coal, containing abundant dull coal and vitrain, semi-bright coal.
Sandy mudstone		0.95	Light gray, with slip surfaces, horizontal bedding, containing carbonaceous mudstone interlayers, RQD=30%.
Coal		0.60	Black, brownish-black streak, dominated by bright coal, containing abundant dull coal and vitrain, semi-bright coal.
Mudstone		0.50	Light gray, with slip surfaces, horizontal bedding, uneven fracture, RQD=10%.
Coarse-grained sandstone		0.60	Grayish white, composed mainly of quartz and feldspar, medium cementation, containing a small amount of gravel, RQD=70%.
Sandy mudstone		1.24	Dark gray, with slip surfaces, horizontal bedding, containing siltstone bands, RQD=60%.
Coal		12.46	Brownish-black streak, dominated by bright coal, containing abundant dull coal and vitrain, semi-bright coal.
Mudstone		0.50	Light gray, easily broken, core short columnar, RQD=45%.
Coarse-grained sandstone		0.90	Dark gray, straight fracture, horizontal bedding, RQD=75%.

Figure 4. Column diagram of drilling hole 3-1 for sand filling.

2.4. Hydraulic Pre-Splitting Technology Scheme for Roof

On the basis of the initial mining top caving control concept and the determination of the fracturing layer, combined with the on-site conditions of the working face, the layout of hydraulic fracturing holes, key technical parameters, equipment selection, and construction technology are determined, and comprehensive safety technical measures are formulated to ensure the safe and efficient implementation of fracturing.

Using the two fixed-end support beams as the mechanical model, based on the mechanical conditions of the rock beam end being pulled apart, combined with the physical

and mechanical parameters of the rock layer, the initial pressure step distance of the direct top and basic top is calculated before and after cracking.

$$\text{Mechanical conditions: } \sigma = [\sigma_t] \tag{2}$$

$$\text{Actual tensile stress at the end of the beam: } \sigma = \frac{M_A}{W} \tag{3}$$

$$\text{Beam end bending moment: } M_A = \frac{qL_0^2}{12} = \frac{(m_1 + m_2)\gamma L_0^2}{12} \tag{4}$$

$$\text{Modulus of beam end section: } W = \frac{m_1^2}{6} \tag{5}$$

Calculation formula for ultimate span (initial step distance):

$$\text{Before cracking: } C_{Z0} = \sqrt{\frac{2m_z[\sigma_{t1}]}{\gamma_Z}} \tag{6}$$

$$C_{E0} = \sqrt{\frac{2m_1^2[\sigma_{t2}]}{(m_1 + m_2)\gamma_E}} \tag{7}$$

$$\text{After cracking: } C_{Z1} = \sqrt{\frac{2m_z[\sigma_{t3}]}{\gamma_Z}} \tag{8}$$

$$C_{E1} = \sqrt{\frac{2m_1^2[\sigma_{t4}]}{(m_1 + m_2)\gamma_E}} \tag{9}$$

In the formula, σ—actual tensile stress of the rock layer, MPa; $[\sigma_t]$—the rock layer allows tensile stress, MPa; M_A—beam end bending moment; W—section modulus at the end of the beam; L_0—ultimate span of beam end cracking, m; m_1, m_2, m_z—rock layer thickness, m; γ_Z, γ_E—average gravity density of direct top and basic top, respectively, N/m^3; C_{Z0}, C_{E0}—initial pressing step distance for direct top and basic top before cracking, respectively, m; C_{Z1}, C_{E1}—initial pressing step distance for direct top and basic top after cracking, respectively, m; $[\sigma_{t1}, \sigma_{t2}]$—allowable tensile stress for direct top and basic top before cracking, respectively, and Pa; $[\sigma_{t3}, \sigma_{t4}]$—allowable tensile stress for direct top and basic top after cracking, respectively, Pa. $m_z =$ 3.2 m, $m_1 =$ 7.6 m, $m_2 =$ 3.9 m, $\gamma_Z =$ 1.4 N/m^3, $\gamma_E =$ 2.8 N/m^3, $\sigma_{t1} =$ 106 Pa, $\sigma_{t2} =$ 236 Pa, $\sigma_{t3} =$ 22 Pa, and $\sigma_{t4} =$ 68 Pa.

The calculation results provide the direct collapse step distance before cracking and the basic collapse step distance. After cracking, the direct collapse step distance and basic collapse step distance are reduced, with a significant decrease in collapse step distance.

The hydraulic fracturing initiation pressure is calculated according to the following formula:

$$\rho_1 = 1.3(3\sigma_3 - \sigma_1 + R_t) \tag{10}$$

In the formula, ρ_1—the starting pressure required for hydraulic fracturing, MPa; σ_1—maximum principal stress at the fracturing point, MPa; σ_3—minimum principal stress at the fracturing point, MPa; and R_t—tensile strength of the roof rock layer at the fracturing point, MPa. Parameter values are calculated based on a maximum burial depth of 403 m, vertical stress = 0.027 × 453 MPa = 10.88 MPa. The lateral pressure coefficient is set to 0.7, with the minimum principal stress. The maximum principal stress $\sigma_3 =$ 12.23 × 0.7 MPa = 7.6 MPa. The tensile strength is taken as 1/10 of the compressive strength (50 MPa), which is 5 MPa. The hydraulic fracturing initiation water pressure is 25.2 MPa, and the pressure is stabilized for 25–30 min during the fracturing process.

The fracturing time is calculated according to the following formula:

$$T = \frac{naBH\pi}{3Q} \tag{11}$$

In the formula, a—crack radius, taken as 10 m; B—crack width, taken as 2 cm; H—crack height, taken as 4.5 m; n—number of cracks, taken as 3; and Q—fracturing device flow rate, taken as 120 L/min. Substituting the parameters into the calculation indicates that the fracturing time for each segment should not be less than 24 min, and the actual value is taken as 25–30 min.

Based on the elliptical shape of hydraulic fracturing with varying fracture height, combined with the principles of linear elastic fracture mechanics and volume conservation, the calculation formulas for fracture radius and borehole spacing are derived. Combined with the on-site parameter values ($Q = 13\ m^3/h$, $T = 30$ min, $E = 5$ GPa, $\sigma = 32$ MPa, $H = 4.5$ m, and k = 0.7), the borehole spacing is calculated to be 11 m. To ensure the quality of fracturing, the actual borehole spacing is taken as 12 m.

2.5. On-Site Application

2.5.1. Construction Plan

Considering that the N4202 working face has completed the installation of comprehensive mining equipment, with the shearer positioned at the locations of supports 1#–14#, hydraulic fracturing boreholes are arranged within a 20 m range of the entry and return airway, totaling 39 boreholes. These include 17 A holes, 17 B holes, 2 C holes at the upper head, and 3 groups of fan-shaped holes at the location of support 14#. Based on the revised site conditions, the specific borehole parameters are as follows in Figure 5.

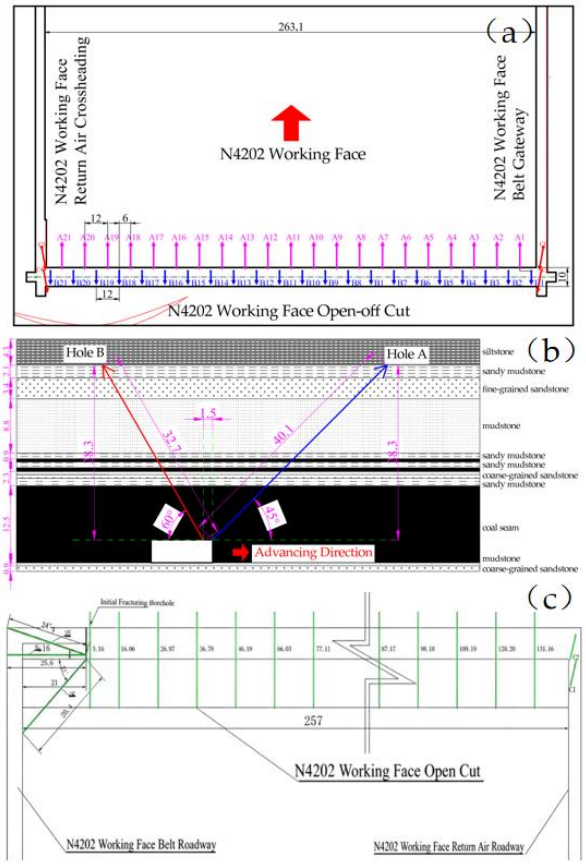


Figure 5. (**a**) N4202 working face cutting, (**b**) N4202 cutting hydraulic fracturing design, (**c**) N4202 cutting hydraulic fracturing drilling change design.

(1) Holes A and B are arranged in parallel, with a drilling spacing of 14 m per group and a hole diameter of 94 mm.
(2) Hole A: Drilled vertically toward the roof ahead of the working face from the coal wall, with the opening position no more than 1 m from the shoulder pocket (avoiding the shoulder pocket), an elevation angle of 45°, and a borehole length of 40 m.
(3) B-hole: Drilled vertically from the coal wall toward the goaf-side roof, with the opening position no more than 2 m from the shoulder pocket, an inclination angle of 60°, and a borehole length of 32 m.
(4) C1 and C2 holes: Located at the end of the airway, with the borehole position 1 m from the coal pillar side, an inclination angle of 45°, directed toward the working face with a deviation angle of 10° relative to the longwall direction, and a length of 26 m.
(5) Fan-shaped holes (3 sets): Located at the 14# support position, the 1# borehole forms a 45° angle with the cutting eye, with an inclination of 42° and a depth of 43.5 m; the 2# borehole forms a 0° angle with the cutting eye, with an inclination of 41° and a depth of 38 m; the 3# borehole forms a 17° angle with the cutting eye, with an inclination of 40° and a depth of 39m. For all boreholes, hydraulic fracturing is applied every 5~7 m of retreat, with each borehole undergoing 5~6 fracturing segments. It should be noted that while hydraulic fracturing can soak the coal body and prevent spontaneous combustion, considering safety concerns such as replacing large pillars in the support system, the top coal is not fractured in this operation.

2.5.2. Construction Process

(1) Before construction, it is necessary to check the connection of the hydraulic fracturing high-pressure pump and high-pressure pipeline. After the inspection is completed, the packer is connected to the water injection steel pipe and a drilling rig is employed to send it into the borehole.
(2) The pressure is slowly increased by turning on the pump, and the packer automatically expands. The maximum pressure of the water pump is recorded, and the pressure is increased for 25–30 min. The pressure changes of the water pump are recorded during the fracturing process and monitored on site.
(3) The pressure is slowly released after 20–30 min of fracturing, the water pump is stopped after the pressure is completely relieved, and the high-pressure pipeline is separated from the water injection steel pipe. After waiting for the water flow in the water injection steel pipe to decrease, the pressure is released from the manual pump. After the water comes out of the borehole, the water injection steel pipe can be disassembled.
(4) The water injection steel pipe is disassembled to retract the packer to the design distance, and steps 1–3 are repeated for subsequent fracturing. After fracturing is completed, the water injection steel pipe is dismantled section by section until the packer is removed.

2.6. Fracturing Performance Evaluation and Fracture Morphology Analysis

To further observe the formation of fractures in the fractured holes and accurately evaluate fracturing performance, this study used the Wuhan Changsheng CXK12 (B) mining borehole imaging instrument (Figure 6) to observe the entire borehole wall of the fractured boreholes. This imaging device has high-definition, real-time imaging and depth positioning functions, which can clearly capture the distribution and morphology of the original structural planes of the borehole wall, fracturing-induced cracks, and fractured areas without drilling or with a small amount of flushing. By analyzing the collected borehole wall expansion map and three-dimensional bar chart, the direction, dip angle,

width, and extension range of the cracks can be intuitively identified, thereby determining whether fracturing has induced an effective complex fracture network and providing a reliable basis for optimizing the subsequent fracturing process parameters.



Figure 6. Mining drilling imager.

The criteria to distinguish natural fractures and hydraulic-induced fractures are defined as follows: (1) natural fractures present irregular morphology, uneven opening, random distribution, and no directional regularity; and (2) hydraulic-induced fractures extend along the borehole axial and inclination direction, with regular shape, uniform opening, and continuous extension. Fractures formed before fracturing with fixed occurrence are defined as natural fractures, while newly generated interconnected fractures after fracturing are identified as hydraulic-induced fractures.

3. Results and Discussion

3.1. Characteristics of Hydraulic Pressure Curve for Top Plate Fracturing

The purpose of hydraulic fracturing on the roof is to induce fracture expansion by applying high-pressure water to the rock mass, thereby achieving pressure relief, and the water pressure curve serves the core metric for reflecting the entire fracturing process and judging fracturing performance. During the fracturing process, it is necessary to carry out fracturing operations for each borehole one by one and to collect and record real-time data on water pressure changes to form a complete water pressure curve. Figure 6 visually presents the overall water pressure evolution law during the top plate fracturing process. Based on the actual fracturing data, it can be seen that the curve clearly presents a dual-stage characteristic of fluctuating cracking and stable expansion. The pressure changes in each stage are closely related to the rock mass response and crack development, providing direct data support for the evaluation of fracturing performance.

From the overall water pressure curve shown in Figure 7, it can be seen that there is a pressure fluctuation period within 100 s after the pump is turned on. During this stage, the pressure fluctuation amplitude is relatively large, and the pressure value repeatedly changes in the range of 23–27 MPa, which is a typical feature before crack initiation. In the initial stage of pump operation, high-pressure water is rapidly injected into the borehole, overcoming multiple resistance factors, such as the tensile strength of the rock mass itself, stress concentration around the borehole, and fracturing fluid filtration. At the same time, the original small cracks inside the rock mass undergo opening and closing movements under the impact of high-pressure water, and their interaction prevents the pressure from stabilizing quickly, resulting in significant fluctuations. This phenomenon is consistent with the basic law of hydraulic fracturing of hard roofs, and the fluctuation amplitude and

duration indirectly reflect the density of the roof rock mass and the development of primary fractures, providing a reference for subsequent adjustment of operational parameters.

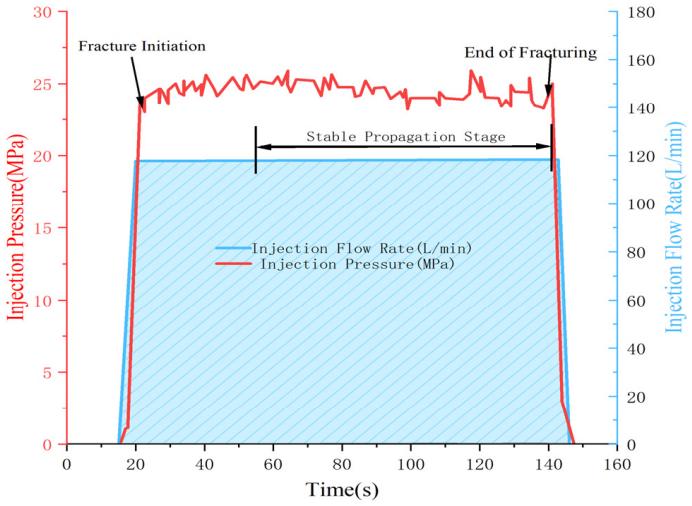


Figure 7. Water pressure curve during top plate fracturing process.

After running the pump for 100 s, the water pressure enters a stable expansion period, gradually stabilizing at around 23 MPa and maintaining a brief stable state. This stage is the critical period for high-pressure water to continue expanding cracks. After the pressure stabilizes, the injection pressure of high-pressure water forms a dynamic equilibrium with the pressure required for crack expansion. The injected high-pressure water continues to penetrate into the interior of the rock mass, pushing the original cracks to continuously extend and expand, while inducing the generation of new cracks, gradually forming a connected crack network and laying the foundation for roof pressure relief. The dual-stage characteristic of the overall curve clearly reflects the interaction process between high-pressure water and the roof rock mass, proving that the pump injection parameter design for this fracturing operation is reasonable and can meet the needs of crack initiation and propagation.

3.2. Comparison of Water Pressure Curves for Each Single Hole and Verification of Fracturing Effectiveness

To further verify the overall effectiveness of roof fracturing and to clarify the differences in fracturing response at different drilling positions, the water pressure curves of each single hole were synchronously recorded during the fracturing process and are presented in Figure 8 (C4 hole, A20 hole, B20 hole, A17 hole, A16 hole, and B15 hole).

From the water pressure curves of each single hole, it can be seen that all boreholes show a trend of initial fluctuation followed by stabilization, which is highly consistent with the overall curve characteristics in Figure 8a–e. This indicates that the fracturing parameters have good universality, and there are no obvious abnormal working conditions during the fracturing process of each borehole. Among them, the pressure fluctuation amplitudes of the C4 hole, A20 hole, and B20 hole are basically consistent with the overall trend, with the fluctuation range concentrated within 23–27 MPa. The stable stage pressure is maintained at around 23 MPa, indicating that the rock mass where these boreholes are located has good uniformity, similar development of primary fractures, and consistent interaction laws between high-pressure water and rock mass during the fracturing process.

Although the overall trend of the water pressure curves for the A17, A16, and B15 holes is consistent, there are slight differences in the amplitudes of local fluctuations, and the duration of some borehole fluctuations is slightly longer. It is speculated that this

is related to the local density and distribution of small cracks in the rock mass at the location of these boreholes. Statistical results of pressure parameters for all 39 fracturing boreholes: the average breakdown pressure is 25.4 MPa (range: 23.1–27.0 MPa, standard deviation = 1.12 MPa), the average propagation pressure is 23.2 MPa (range: 22.5–24.1 MPa, standard deviation = 0.68 MPa), and no obvious closing pressure is detected during stable fracturing stage. The pressure data of each borehole display low dispersion, which proves the consistency of the fracturing performance.

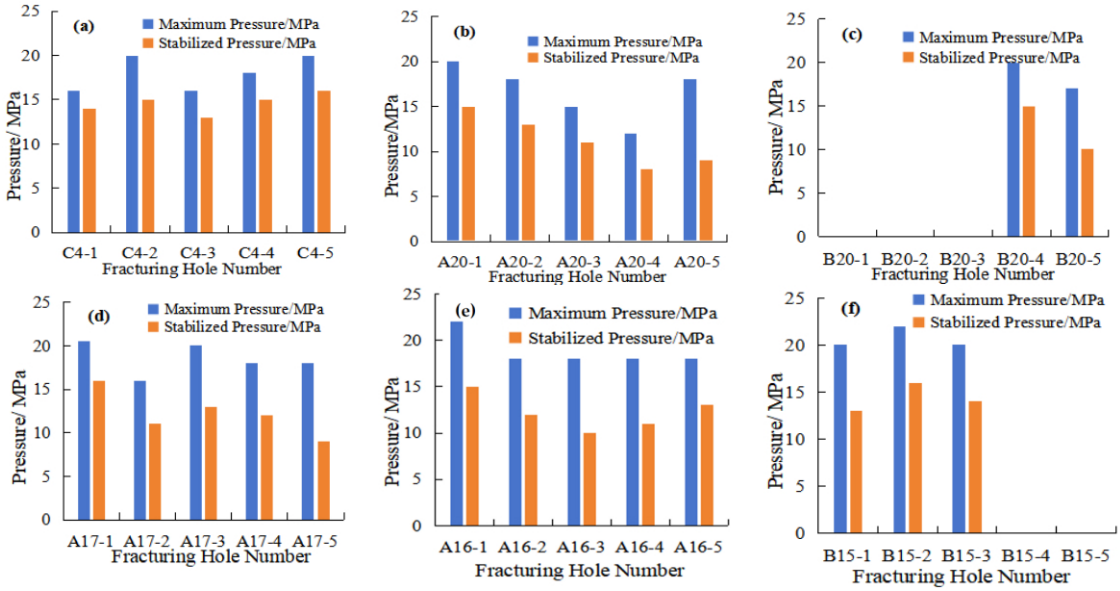


Figure 8. (**a**) Water pressure of C4 fracturing hole, (**b**) Water pressure of A20 fracturing hole, (**c**) Water pressure of B20 fracturing hole, (**d**) Water pressure of A17 fracturing hole, (**e**) Water pressure of A16 fracturing hole, (**f**) Water pressure of B15 fracturing hole.

3.3. Morphology of Water Pressure Cracks on the Roof

In order to accurately observe the formation of cracks in the fractured holes, the Wuhan Changsheng CXK12 (B) mining borehole imaging instrument was used to conduct systematic observations and detect fractured boreholes, providing a visual basis for the evaluation of fracturing performance. A total of 18 fracturing boreholes were observed this time, accounting for 46% of the total number of fracturing boreholes. A comparative analysis of Figure 9 (pre-fracturing borehole view) and Figure 10 (post-fracturing borehole view of fractures) clearly reveals the impact of fracturing on crack development.



Figure 9. Images of drilling holes before fracturing.

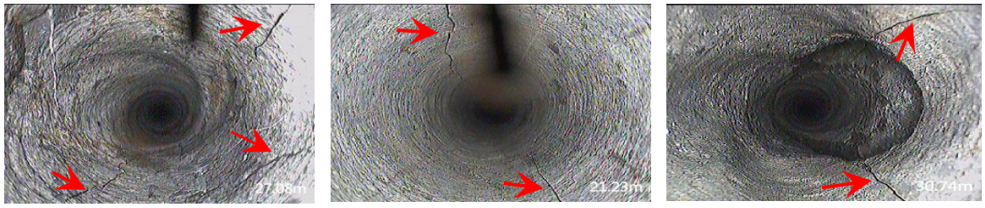


Figure 10. Microscopic observation of cracks inside the holes after fracturing.

The borehole imaging results showed that 17 out of 18 borehole had obvious fractures after fracturing, accounting for 94%, indicating a very high success rate of fracturing. On-site observations revealed dense and uniform effective cracks distributed in both the circumferential and longitudinal directions of the borehole wall. The number of cracks in a single borehole is $\geq$8, and the angle of the cracks is basically the same as the inclination angle of the borehole. The crack opening is uniform, with a measured width of 0.8–2.2 mm.

Quantitative statistical results of fracture parameters: the average linear fracture density is 2.12 pieces/m (standard deviation = 0.27), the average fracture aperture is 1.46 mm (standard deviation = 0.19 mm), and the overall fracture connectivity index of all monitoring boreholes reaches 92.3%, which is consistent with the water conduction test results.

At the same time, there is no obvious collapse or block falling phenomenon in the rock mass of the borehole wall. Only local mudstone layers exhibit reduced imaging clarity due to the characteristics of the rock mass. The overall regularity of the borehole wall is over 90%, and no primary fractures or dissolved pores larger than 2 mm are observed, ruling out the interference of existing fractures on fracturing performance. Clear fracturing-induced marks can be seen on the borehole wall, and the original rock stress is evenly released. The rock mass has not undergone excessive fragmentation (fragmentation size > 5 cm), and the integrity of the rock mass around the cracks remains intact. There is no rock collapse or structural instability caused by fracturing. Figure 9 clearly shows high-quality fractures with high density, high connectivity, and large openings, confirming that the fracturing performance meets the design expectations.

To further verify the uniformity and stability of the fractures, typical boreholes such as A4, A9, A11, A13, B2, B5, and B20 were selected for focused observation analysis. Combined with the observation results of each single hole in Figure 11a–g, the distribution position, morphological characteristics, and development rules of single-hole fractures were accurately analyzed, providing refined support for the overall fracturing performance. The formed dense hydraulic fractures with an opening of 0.8–2.2 mm fundamentally destroy the overall integrity of the hard roof. The high-density interconnected fracture network cuts the intact rock mass into multiple discrete rock blocks, breaking the continuous bearing structure of the roof. Meanwhile, the cracks reduce the effective bearing area of the rock mass and introduce numerous weak structural planes, which significantly decrease the overall mechanical strength, including the tensile strength and compressive strength of the hard roof. Larger crack openings further weaken the friction and occlusion effects between rock blocks, making the roof more prone to sequential collapse under mining-induced pressure, rather than forming a large, suspended roof with high elastic energy accumulation.

In Class A drilling, the observation results of the A4 hole (Figure 11a) show that the cracks are concentrated at three key positions: 16.92 m, 17.78 m, and 22.27 m. The crack morphology is regular, the main crack is clear, and the secondary cracks are evenly developed without isolated cracks. They are symmetrically distributed with the axial direction of the drilling hole, and the expansion length meets the standard of 0.5–1.2 m, confirming that the fracturing stress release in this section is uniform. The cracks in the A9 hole (Figure 11b) are concentrated at 24.5 m, 26.12 m, and 29.06 m, with continuous crack extension and no closure or sharp out phenomenon, consistent with the development pattern of the A4 hole, indicating the stability of the A-type drilling fracturing process. The A11 hole (Figure 11c) shows clear cracks at 18.35 m, 20.09 m, and 20.83 m, with uniform spacing and obvious symmetrical distribution characteristics. The secondary cracks are well connected to the main cracks, further verifying the consistency of the fracturing performance of Class A boreholes. The cracks in the A13 hole (Figure 11d) are distributed

at 18.69 m, 19.04 m, and 28.27 m. Although the distribution positions are slightly different, the crack morphology and expansion length meet the design requirements, and there is no abnormal development phenomenon. In Class B boreholes, there are 3 obvious cracks in each of the B2 and B20 boreholes (Figure 11e,g), which are distributed along the axial direction of the borehole. Although the specific depth is not marked, the shape is regular and the connectivity is good, and the extension length is controlled within the range of 0.5–1.2 m. The B5 hole (Figure 11f) forms cracks at 16.2 m, 22.27 m, and 25.9 m, which are consistent with the symmetrical distribution characteristics of multiple sections in Class A boreholes, and the crack opening is uniform without any rock collapse phenomenon. Overall, the typical single-hole observation results meet the design standards, verifying the stability and reliability of the fracturing process.

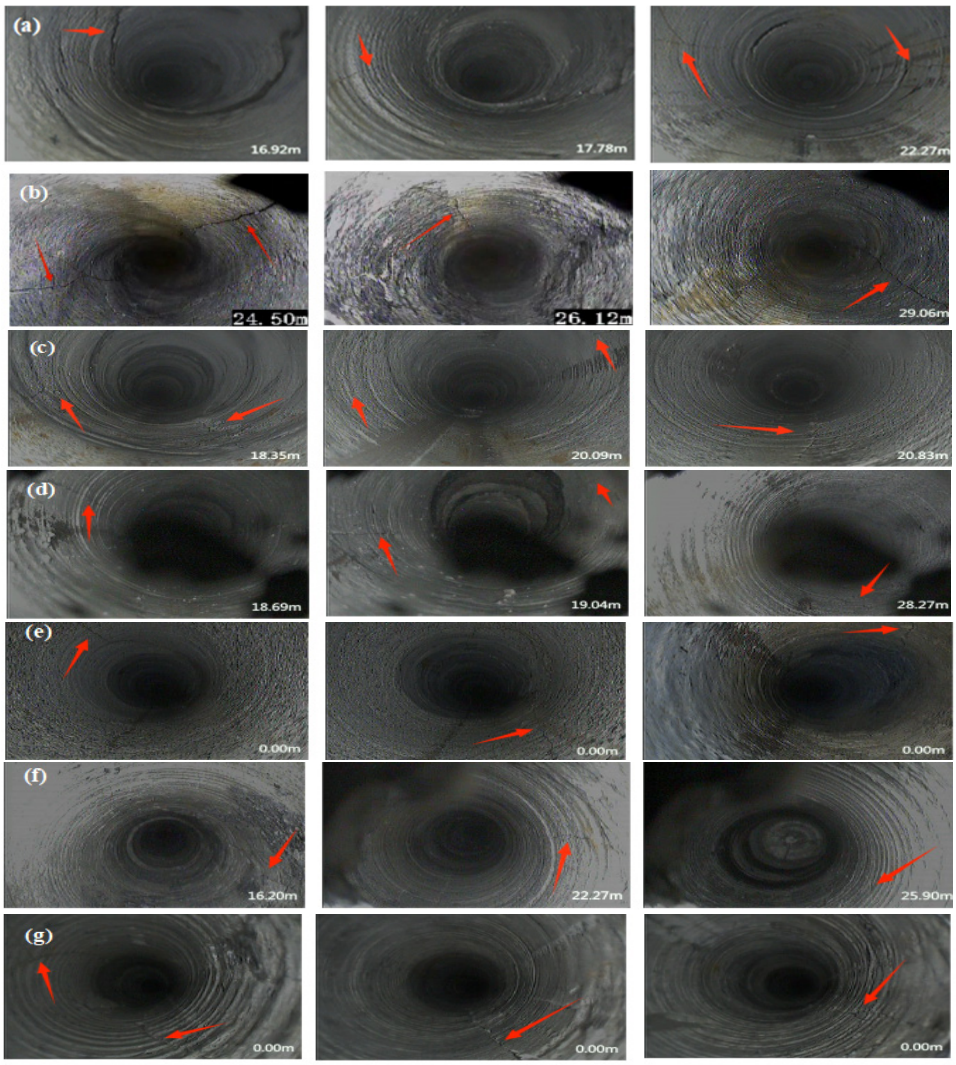


Figure 11. (**a**) A4 hole borehole imaging results, (**b**) A9 hole observation results, (**c**) Observation results of A11 hole, (**d**) A13 hole borehole imaging results, (**e**) B2 hole observation results, (**f**) B5 Hole borehole imaging results, (**g**) Observation results of B20 hole.

3.4. Evaluation of Collapse Effect After Top Plate Fracturing

The collapse of the roof is a core indicator for evaluating the effectiveness of hydraulic fracturing and determining the stability of the roof. Combining Table 3 and Figure 12, the roof collapse of the goaf after hydraulic fracturing can accurately analyze the impact of fracturing on roof collapse and clarify the characteristics of roof activity after fracturing. Through the analysis of the roof collapse, it can be concluded that compared to not adopting

mandatory roof caving measures, the initial mining roof caving step distance (large-scale roof collapse) of the working face is reduced to 13.2 m. The shortening of the roof caving step distance effectively avoids the large-scale accumulation of energy in the roof and reduces the risk of sudden roof collapse.

Table 3. Roof collapse of goaf after hydraulic fracturing in N4202 working face of Sandunzi coal mine.

Time	Head Propulsion (m)	Tail Propulsion (m)	Collapse of the Roof in the Goaf Area
22 November 2025	9.3	4.4	22 to 40 roof collapses
23 November 2025	11.6	5.7	40 to 78 roof collapses
25 November 2025	17.3	9.1	78 to 126 roof collapses
26 November 2025	18	11.3	126 to 135 roof collapses
27 November 2025	23.4	16.2	12 to 22 hydraulic shields, 135 to 148 hydraulic shields with roof collapse
28 November 2025	24.4	17.2	From frame 1 to frame 12, the lower headboard has collapsed, and the upper headboard has not collapsed sufficiently (in the triangular area)
29 November 2025	30	22.6	Upper head collapse

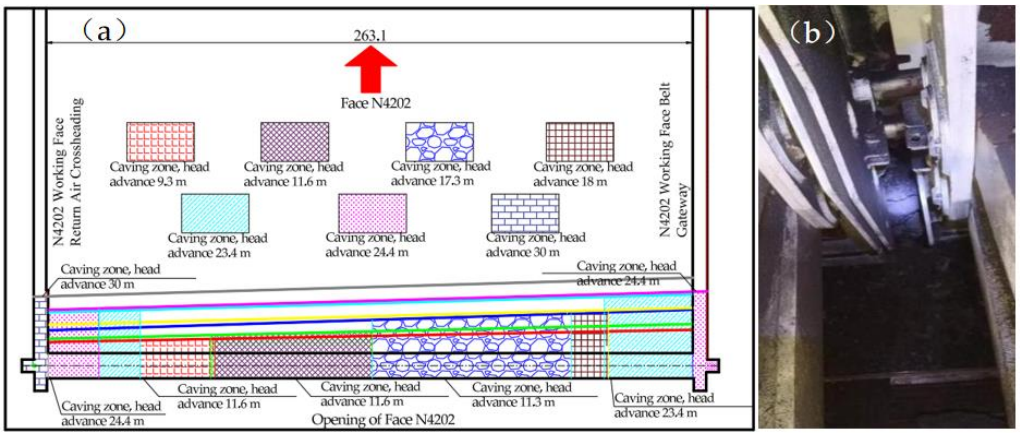


Figure 12. (**a**) The collapse state of the goaf roof after hydraulic fracturing in the working face; (**b**) Scenario of roof collapse of goaf after hydraulic fracturing in working face.

Based on Table 3, it can be seen that the top plate of the goaf collapses in stages after fracturing. As the distance between the head and the tail of the machine increases, the top plate of the goaf collapses in sequence according to the frame section, gradually extending from a specific frame section to the entire working face. There is no large-scale sudden collapse phenomenon, and the overall mining pressure tends to ease. This is highly consistent with the roof collapse scene presented in Figure 12, which clearly shows the orderly collapse of the top plate of the goaf after fracturing, without obvious large-scale collapse traces, further confirming the characteristics of segment-by-segment collapse. During the initial mining period, there are no significant increases in drilling stress and microseismic monitoring data, which remain at low levels and confirm the collapse of the roof. This indicates that after hydraulic fracturing, the mechanical properties of the roof are effectively weakened, the integrity of the roof decreases, and the roof activity tends to ease, without stress concentration or energy accumulation. In summary, hydraulic fracturing effectively optimizes the collapse form of the roof, achieves smooth collapse of the roof section by section, eases the manifestation of mining pressure, and provides a reliable guarantee for operational safety during the initial and recovery periods of the working face.

Shortening the initial roof caving step is closely linked to the controlled release of the elastic potential energy of the surrounding rock. A large natural caving step means that

a hard roof forms a long-span overhanging structure, which continuously accumulates massive elastic potential energy under overburden pressure. By shortening the caving step, hydraulic fracturing limits the overhang range of the roof, and the scale of the rock beam bearing load is reduced accordingly. The elastic potential energy stored in the roof and surrounding rock is released continuously and slowly along with staged roof collapse, rather than being accumulated in a large area. This working mechanism fundamentally avoids the instantaneous violent energy release caused by the sudden overall collapse of the long-span hard roof and effectively suppresses the occurrence of rockburst disaster driven by sudden energy explosion. Combined with the field monitoring results in this study, the shortened caving step and staged collapse maintain a stable stress field in the working face, which is the core control mechanism for rockburst prevention in this engineering practice.

3.5. On-Site Experimental Testing

In order to reduce the dynamic pressure impact on the main roadway, such as the return air roadway, during the final stage of the N4107 mining face, hydraulic pre-splitting boreholes were constructed in advance to separate the roof structure, cut off the stress transmission channel, and thus achieve pressure relief and roadway protection. After on-site implementation, the effectiveness of pressure relief was tested from multiple perspectives using specific indicators.

First, from the perspective of drilling and fracturing effects, cracks have significantly developed on the borehole wall. The water injection volume of each borehole exceeds 30 m^3, and the water injection pressure is maintained between 20 and 30 MPa, indicating that the roof rock layer is fully fractured. After fracturing, a drilling sight found 1–3 axial cracks on the hole wall, confirming that hydraulic pre-fracturing successfully achieved effective separation of the roof structural plane and laid the foundation for cutting off the stress transmission path. Second, in terms of the mine pressure in the return air channel, the pressure relief effect is significant. By carrying out hydraulic top cutting and pressure relief work, the bottom bulge of the return airway in the N4107 working face has been effectively controlled, with an average bottom bulge reduction of 300–400 mm. At the same time, the convergence of the slope is also significantly reduced; specifically, the convergence of the mining slope is reduced by more than 230 mm. This indicates that top cutting and pressure relief effectively weaken the squeezing effect of mining stress on the surrounding rock of the return airway, greatly improving the overall stability of the return airway. The microseismic monitoring data indicate that the intensity of energy release caused by mining has been significantly decreased, according to the data obtained from the KJ551 microseismic monitoring and early warning system installed on the N4107 working face. After the construction of six fracturing boreholes in the return air channel, the daily microseismic energy and frequency decrease by more than 50%, and no microseismic high-energy events exceeding 2000 J re-occur. The area affected by microseismic advance also decreases (Figure 13). This further demonstrates that hydraulic fracturing effectively suppresses large-scale sudden roof fractures and reduces the risk of dynamic pressure in the mining area. Finally, the observation results within the return airway show that although the overall pressure relief is effective, there is still a certain degree of residual mine pressure. When the distance between the mining face and the stopline is 15 m, some slurry leakage is observed in the return airway. As the mining face advances to the stopline position, the degree of cracking in the slurry layer of the roadway increases, and the local bottom bulge reaches 100–200 mm. However, there is no significant roof subsidence or deformation of the two sides of the roadway, indicating that the top cutting and pressure relief measures largely protect the structural integrity of the return airway, with only slight surface damage.

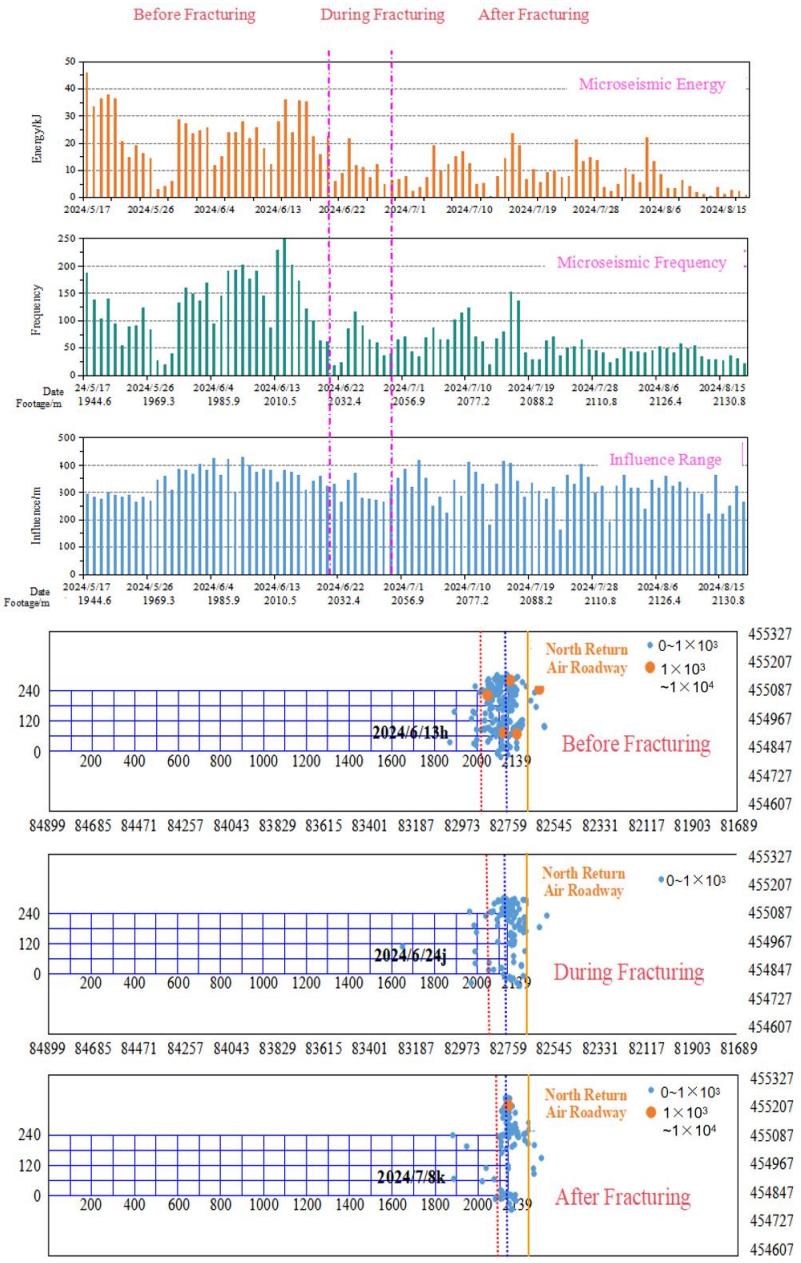


Figure 13. Analysis of microseismic events before and after fracturing.

The variations in fracturing water pressure and injection flow rate with time during the single-hole hydraulic fracturing process is shown in Figure 14. In the early stage of hydraulic fracturing, the water injection pressure rapidly increases. When it reaches about 27 MPa, the borehole begins to crack, and the water pressure curve briefly drops and then quickly stabilizes. At this time, the flow rate also reaches the set value. During the approximately 40 min fracturing process, the water injection pressure remains stable at around 27 MPa with minimal fluctuations, and the water injection flow rate remains stable at 120 L/min. This indicates that the cracks continuously and steadily expand forward, forming smooth water channels, and the fracturing operation enters a stable expansion period. After the water injection stops, the pressure and flow rate quickly decrease to zero synchronously, marking the end of the fracturing process. Overall, the curve shape is typical, indicating that the fracturing operation successfully achieves the stable expansion of drilling initiation and cracks, with good control of the process parameters, providing a reliable guarantee for the subsequent top cutting and pressure relief effect.

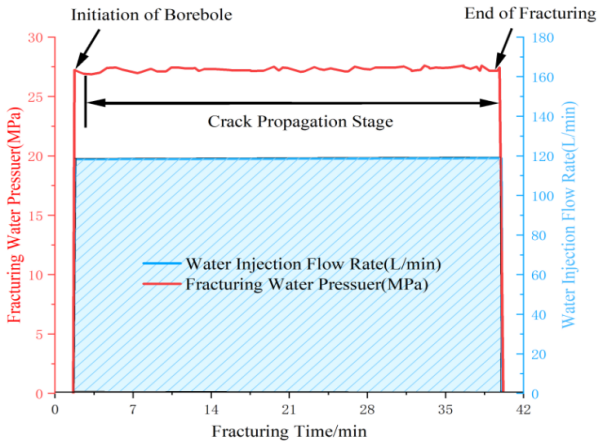


Figure 14. The variation law of fracturing water pressure and injection flow rate with time during the single-hole hydraulic fracturing process.

3.6. Microseismic Patterns in Top Plate Fracturing Layers

The adopted KJ1222 microseismic monitoring system uses P-wave velocity = 3800 m/s, S-wave velocity = 2100 m/s as the unified rock velocity model. The system positioning accuracy is within ±8 m, and the effective energy detection threshold is 10 J. A total of 12 geophones are deployed in a 3D network layout: 6 sensors in the return airway, 4 sensors in the belt roadway, and 2 sensors near the open-off cut, realizing full coverage of the monitoring area. During the fracturing period, the microseismic monitoring system detects a total of 40 microseismic events, with a maximum microseismic energy of 494 J and a total microseismic energy of 1960 J. The 95% confidence intervals of the growth rates for microseismic frequency and energy are 271–299% and 218–242%, respectively. The Mann–Whitney U test was carried out on the microseismic data before and after fracturing, yielding $p < 0.01$, which indicated that the differences in microseismic frequency and energy are statistically extremely significant.

The variation law of microseismic frequency and energy is highly coupled with the evolution process of hydraulic fractures. In the early stage of pressurized water injection, high water pressure acts on the borehole wall, overcoming the tensile strength of the surrounding rock and inducing initial micro-cracks. A large number of tiny rock ruptures occur inside the roof strata, resulting in a sharp rise in the frequency and energy of microseismic events. In the fracture propagation stage, with the continuous injection of high-pressure water, the initial cracks gradually expand, extend, and interconnect to form a fracture network. Rock mass damage continues to develop, so microseismic activity remains at a high level.

After hydraulic fracturing is finished, the water pressure is released and no new cracks are generated. The formed fracture network tends to be stable and the rock mass stops large-scale rupture; thus, the frequency and energy of microseismic events decrease rapidly and gradually return to a stable state. After fracturing is completed, the microseismic activity tends to stabilize, and the frequency of microseismic events obviously decreases. After fracturing, the microseismic monitoring system detects a total of 5 microseismic events with a total energy of 218 J and a maximum energy of 189 J. The microseismic profile analysis reveals that the microseismic energy is distributed in the sandstone layer 30–40 m above the coal seam roof, intuitively reflecting the interaction process between high-pressure water and the roof rock mass.

Based on the microseismic monitoring plan and microseismic event cloud maps in Figure 15a–e, it can be seen that the frequency and energy of microseismic events before fracturing are low. Figure 15a clearly shows the sparse distribution of microseismic

activity before fracturing. During the fracturing process, there is a significant increase in the frequency of microseismic events and an increase in their energy. The microseismic distribution density in Figure 15b is significantly higher than before fracturing, confirming the active role of high-pressure water in creating and expanding fractures during the fracturing process. After fracturing is completed, Figure 15c shows that the microseismic activity tends to flatten out and the distribution of microseismic events is sparse, indicating that the fractures generated by fracturing have stabilized and developed. Figure 15d,e show the overall distribution characteristics of microseismic activity during the mining period, providing a visual basis for the subsequent analysis of roof stability during mining.

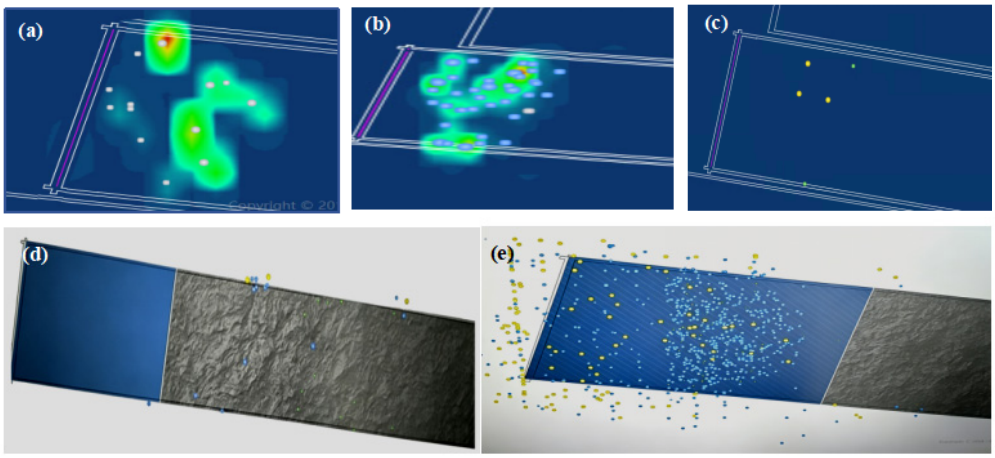


Figure 15. (**a**) Microseismic monitoring plan before fracturing from 1–24 September; (**b**) Microseismic monitoring plan during the fracturing period from 25 September–18 October; (**c**) Microseismic monitoring plan during the fracturing period from 19–28 October; (**d**) Cloud map of microseismic events in November 2025; (**e**) Cloud map of microseismic events in December 2025.

During the mining period, continuous microseismic monitoring was carried out on the N4202 working face. By combining various microseismic data charts from Figure 16, the distribution pattern and energy characteristics of microseismic events during the mining period can be accurately analyzed. The monitoring data show that during the mining period, the frequency of microseismic events shows a phased increasing trend with the intensification of mining activities. The maximum number of microseismic events in a single event reaches 123, with a maximum microseismic energy of 4.56 KJ. The cumulative maximum energy for the day reaches 147.64 KJ, and the coordinates of the epicenter are X: 31455990, Y: 4786004, Z: 772. Figure 16a,b clearly show the trend of changes in the number of microseismic events, total energy, and maximum energy during the initial mining period, and Figure 17c,d show the frequency and energy changes of microseismic events in the later stage of mining, showing an overall trend of increasing frequency and stable energy.

According to the statistical results of microseismic data and Figure 17, although mining has intensified the speed of rock fracture and fragmentation of the working face roof, hydraulic fracturing has successfully cut off the hard rock layer overlying the No. 4-1 coal seam by generating a large number of water pressure cracks, effectively reducing the integrity of the roof, weakening the mechanical properties of the roof, promoting timely fracture and collapse of the roof, and improving the stress environment of the working face. During the mining period, the daily occurrence frequency of microseismic events is relatively stable, without concentrated outbreaks, and there are no high-energy events. The maximum energy is only 4.56 KJ, and there is no risk of impact, indicating that the fracturing effect continues to play a role.

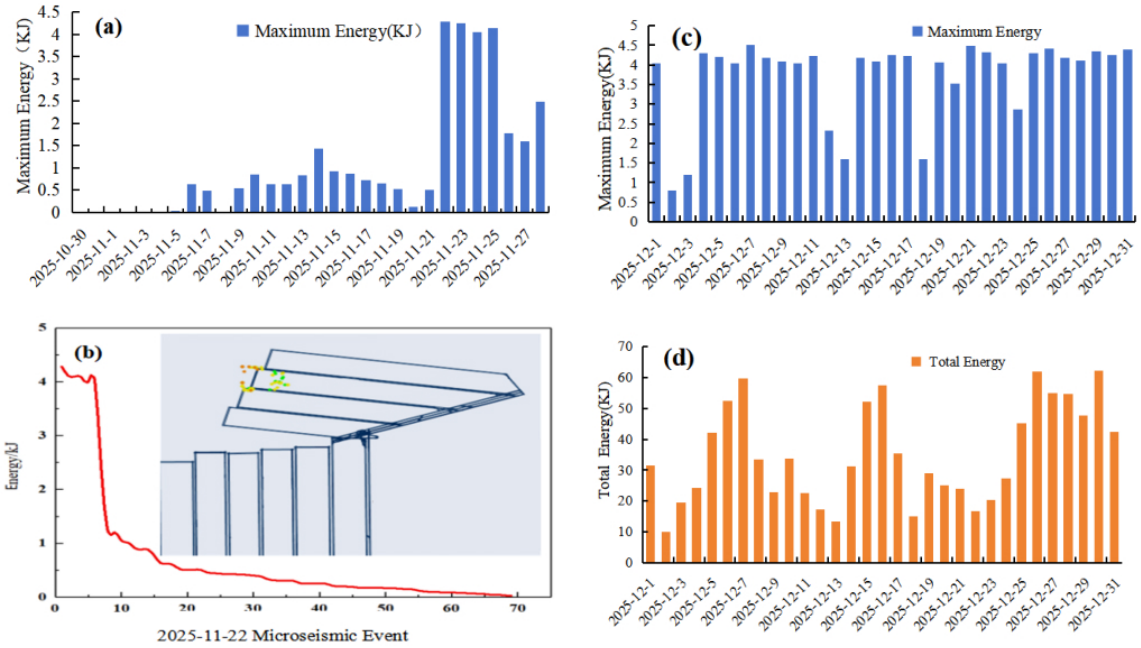


Figure 16. (**a**) Number and maximum energy of microseismic events during the mining period from 30 October to 28 November; (**b**) Total and maximum energy of microseismic events during the mining period from 30 October to 28 November; (**c**) Number and maximum energy of microseismic events during the mining period from 1 December to 31 December; (**d**) Total energy of microseismic events during the mining period from 1 December to 31 December.

Based on the data obtained from the KJ1222 microseismic monitoring and early warning system on the N4202 working face, a comprehensive analysis was conducted on the hydraulic fracturing performance and roof stability during the mining period. It is known that during the hydraulic fracturing period, the microseismic response is significant, indicating effective creation and expansion of fractures. During the fracturing period, a total of 40 microseismic events are monitored, with a total energy of 1960 J and a maximum microseismic energy of 494 J. Compared to before fracturing, the total frequency of microseismic events increases by 285%, the total energy increases by 230%, and the maximum microseismic energy per event increases by 41.1%. Based on the microseismic profile and the microseismic monitoring plan during the fracturing period in Figure 17a,b, the microseismic energy is mainly distributed in the sandstone layer 30–40 m above the coal seam roof, indicating that during the hydraulic fracturing process, high-pressure water successfully achieves active fracturing and expansion, triggering a large number of micro fractures in a short period of time, which verifies the effectiveness of fracturing on the roof rock layer.

Hydraulic fracturing effectively weakens the mechanical properties of the roof, reducing its integrity and promoting its timely fracture and collapse. After fracturing is completed, the frequency of microseismic events decreases to 5 times, with a total energy of 218 J and a maximum energy of 189 J. Combined with the microseismic monitoring plan after fracturing, it can be seen that microseismic activity tends to stabilize, indicating that the water pressure cracks generated by fracturing have effectively cut off the hard rock layers overlying the No. 4-1 coal seam, weakening the mechanical strength of the roof and breaking the integrity of the original roof. This creates the conditions for timely fracture and collapse of the roof, effectively improving the stress environment of the working face and reducing the risk of rockburst.

Microseismic data verification in Figure 17c,d shows that the fracturing effect remains stable and effectively controls the risk of impact. In this period, although the frequency of

microseismic events shows a phased increasing trend with the intensification of mining, the distribution of microseismic events is relatively stable and there is no concentrated outbreak phenomenon. The maximum microseismic energy during the period is only 4.56 KJ, and no high-energy microseismic events occur. These findings indicate that the water pressure cracks formed by hydraulic fracturing continue to play a role, effectively controlling the severity of roof rock fracture and fragmentation and further consolidating the effect of stress environment improvement. Consequently, there is no risk of impact throughout the entire process, ensuring the safe progress of mining work in the working face.

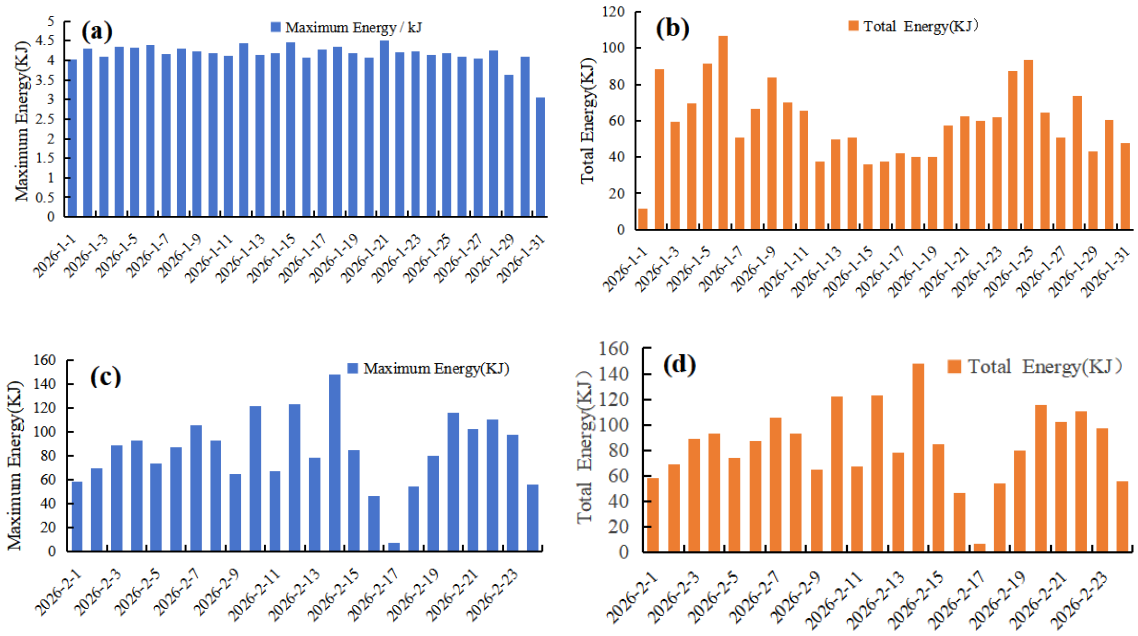


Figure 17. (**a**) Number and maximum energy of microseismic events during the mining period from 1 to 31 January; (**b**) Total energy of microseismic events during the mining period from 1 to 31 January; (**c**) Number and maximum energy of microseismic events during the mining period from 1–24 February; (**d**) Total energy of microseismic events during the mining period from 1–24 February.

Overall, hydraulic fracturing of the N4202 working face has achieved the expected goals and the fracturing effect is significant. By using high-pressure water to create and expand fractures, the overlying hard rock layers are successfully cut off, weakening the mechanical properties of the roof and reducing its integrity. This promotes timely and stable fracture and collapse of the roof, effectively improving the stress environment of the working face and controlling the risk of impact ground pressure throughout the entire process. This provides a reliable guarantee for operational safety during the initial and recovery periods of the working face.

3.7. Hydraulic Fracturing Mechanism

The mechanism of hydraulic fracturing in this study mainly includes two parts: a rock breaking mechanism and an impact ground pressure prevention mechanism. The aim is to destroy the integrity of the roof and weaken its mechanical strength through the action of high-pressure water, thereby promoting the timely and stable collapse of the roof and reducing the risk of impact. The mechanism of rock breaking can be divided into three stages: the stage of crack initiation, where high-pressure water is injected into the borehole until the pressure reaches the tensile strength of the rock formation and initial cracks are generated in weak areas of the borehole wall. During the crack propagation stage, high-pressure water maintains a stable pressure, causing the initial cracks to propagate along the direction of maximum principal stress and the weak surface of the rock formation, forming

a connected crack network. In the stable fracturing stage, the decrease in water pressure tends to stabilize, a crack network forms, the mechanical strength of the roof significantly decreases, and it can collapse smoothly. The mechanism of preventing and controlling rockburst mainly manifests in three aspects: first, the integrity of the roof is reduced, a dense network of cracks forms, and the continuity of the rock layer is damaged; second, the mechanical properties of the roof are weakened, and the combination of high-pressure water immersion and crack formation significantly reduces the strength of the rock layers; and third, the stress environment is improved, promoting timely collapse of the roof by releasing elastic potential energy and alleviating stress concentration.

In terms of the roof pressure relief mechanism, after formation of the interconnected fracture network, the stress transfer path inside the hard roof is cut off. The high elastic potential energy accumulated in the intact rock mass is gradually released through the expansion and sliding of fractures, instead of being concentrated in local areas. With the advance of the working face, the pre-fractured roof collapses step by step in a small range, and the overburden pressure is uniformly transferred to the surrounding rock and support system. The overall stress level of the working face roof is continuously reduced, the stress gradient becomes gentle, and the risk of sudden energy release and rockburst induced by a large-area suspended roof is effectively eliminated.

In-situ monitoring of the N4202 working face shows that after fracturing, there are $\geq$8 single-hole cracks, and the tensile strength of the rock layer significantly decreases. The microseismic activity tends to stabilize, fully confirming the effectiveness of hydraulic fracturing mechanism.

3.8. Comparison with Conventional Rockburst Prevention Technologies and Novelty

To further illustrate the advantages of the proposed technology, a comprehensive comparison among roof hydraulic fracturing, blast pre-splitting, and water injection for roof softening is conducted regarding construction cost, safety risk, vibration influence, and operation complexity, as shown below:

Construction cost: Water injection for roof softening < Hydraulic fracturing < Blast pre-splitting.

Safety and vibration: Hydraulic fracturing produces slight vibrations with no secondary disaster risk, which is far safer than blast pre-splitting, and water injection for roof softening causes no vibrations but limited applicability.

Operation complexity: Water injection for roof softening is the simplest, blast pre-splitting requires strict approval, and hydraulic fracturing has moderate procedures and strong controllability.

In terms of research novelty: Different from most single-monitoring studies, this work adopts an integrated multi-method field verification system, combining borehole imaging (direct fracture observation), full-period microseismic monitoring (dynamic energy monitoring), and on-site roof collapse observation (macro effect evaluation). This multi-dimensional detection effectively guarantees the objectivity and comprehensiveness of the test results, which is the main innovation of this study.

4. Conclusions and Prospect

4.1. Conclusions

In response to the difficulty of preventing and controlling the impact ground pressure of the hard roof slab in the N4202 thick coal seam fully mechanized caving working face, a study on hydraulic fracturing of hard roof slabs was carried out through on-site geological investigation, technical scheme design, on-site fracturing, and multi-dimensional evaluation. The following main conclusions can be drawn:

(1) The roof and floor of coal seam No. 4-1 in the N4202 working face are mainly composed of hard sandstone. The sandstone in the old roof has strong integrity and is difficult to collapse, making it the main control object of rockburst. The cutting hole is supported by a combination of anchor rods, anchor cables, steel strips, steel reinforcement beams, and mesh plates. The support parameters are reasonable and can meet the safety requirements of hydraulic fracturing and working face mining.
(2) Based on the principle of filling the goaf, the initial mining top caving control method was designed to artificially create cracks, damage the integrity of the roof, promote its timely collapse, and improve the stress environment. The fracturing height was calculated and determined to be 19 m, with a focus on directly fracturing the immediate roof and the old roof, providing a theoretical basis for the design of hydraulic fracturing schemes.
(3) The key technical parameters of hydraulic fracturing were optimized and determined: the initial pressure step distance after cracking is 10 m, the basic top is 15.6 m, the starting water pressure is 25.2 MPa, each fracturing time is 25–30 min, and the drilling spacing is 12 m. A layout plan for 39 fracturing boreholes was designed, including A holes, B holes, end C holes, and fan-shaped holes. The fracturing process was standardized and no safety accidents occurred.
(4) Multi-dimensional evaluation showed that hydraulic fracturing can effectively destroy the integrity of the hard roof, promote its timely and stable collapse, and significantly reduce the risk of rockburst. After fracturing, the microseismic activity is stable without high-energy events and the step distance of roof collapse is significantly reduced, with even fragmentation.

This study presents an overall design integrating A-type, B-type, C-type, and fan-shaped boreholes, with a total of 39 fracturing holes at a target depth of 19 m. By combining borehole imaging, microseismic monitoring, and field observations, the effectiveness of hydraulic fracturing is quantitatively verified from multiple dimensions. The optimized technical scheme can effectively weaken hard roof integrity, reduce caving step distance, and eliminate rockburst risk, which has prominent application value for the initial mining safety of thick coal seams under hard roof conditions.

4.2. Limitations and Future Work

While this study achieved good on-site performance, several limitations and follow-up research directions are summarized as follows:

Long-term evolution of fracture permeability: This study only tested the fracture state in the short term after fracturing. The long-term changes in fracture permeability under repeated mining disturbances were not analyzed, which warrant further long-term field monitoring.

Geochemical interaction with clay-rich strata: The study area contains partial clay-rich interlayers. The water–rock geochemical interactions between fracturing fluid and clay strata, as well as their influence on fracture stability, are not discussed in this paper.

Scalability for different pressure regimes: The current technical scheme is optimized for the in-situ stress of this working face. The adaptability and parameter adjustments under different high- and low-pressure regimes need to be explored in subsequent research.

Fracturing height discrepancy: The theoretical fracturing height (41.5 m) calculated using the ideal goaf-filling formula is quite different from the actual construction height (19 m). The empirical formula for layered fracturing of composite roofs needs to be further expanded.

In future research, we will carry out long-term monitoring of fracture characteristics, explore water–rock interaction laws, and optimize the theoretical calculation formula for fracturing height of composite hard roofs.

Author Contributions: Conceptualization, J.L.; Methodology, J.L.; Formal analysis, K.X.; Data curation, K.X.; Visualization, K.X.; Image processing, K.X.; Investigation, X.L.; Field tests, X.L.; On-site hydraulic fracturing, X.L.; Validation, X.L.; Microseismic monitoring tests, N.L.; Resources, N.L.; Project administration, N.L.; Literature collection, P.W.; Preliminary data sorting, P.W.; Writing—review and editing, J.L. and P.W.; Supervision, J.L.; Funding acquisition, J.L. All authors have read and agreed to the published version of the manuscript.

Funding: The research described in this paper was financially supported by the National Natural Science Foundation of China (No. 52574258) and the Natural Science Foundation of Shandong Province (ZR2024ME097).

Data Availability Statement: The original contributions presented in this study are included in the article. Further inquiries can be directed to the corresponding author.

Conflicts of Interest: The authors declare no conflict of interest.

References

1. Cai, Y.; Yan, B.; Zhang, C. Dust transport and diffusion under individual and coupled dust source conditions in a fully mechanized coal mining face. *Granul. Matter* **2026**, *28*, 41. [CrossRef]
2. Li, Y.; Yan, H.; Zheng, H. Negative Pressure Dust Reduction Technology and Dust Diffusion Characteristics of the Fully Mechanized Coal Mining Face. *Min. Metall. Explor.* **2025**, *43*, 305–321. [CrossRef]
3. Qin, K.; Shu, L.; Chen, Z. Abnormal Pressure Event Recognition and Dynamic Prediction Method for Fully Mechanized Mining Working Face Based on GRU-AM. *Sensors* **2025**, *25*, 7336. [CrossRef] [PubMed]
4. Yuan, G.; Ma, L.; Sun, J. Study on Air Leakage Law and Coal Spontaneous Combustion Danger Area in Goaf of Ultra-Long Fully Mechanized Mining Faces with Large Mining Height. *ACS Omega* **2025**, *10*, 34160–34175. [CrossRef] [PubMed]
5. Zhao, J.; Yu, H.; Dong, H. Analysis on dust prevention law of new barrier strategy in fully mechanized coal mining face. *Process Saf. Environ. Prot.* **2024**, *187*, 1527–1539. [CrossRef]
6. Yang, R.; Xu, Y.; Chen, P. Numerical study on rockburst induced by spalling-structural buckling in surrounding rock with vertically parallel joints of deep hard-brittle large-section square tunnel under cyclic loading-unloading. *J. Dyn. Disasters* **2026**, *2*, 100067. [CrossRef]
7. Liu, S.; Zhang, J.; Lin, Z. Assessment of rockburst proneness in thermally-damaged fractured granite: A quantitative analysis of energy evolution and strain localization intensity. *Theor. Appl. Fract. Mech.* **2026**, *145*, 105677. [CrossRef]
8. Zhao, M.Y.; Ge, C.Z.; He, G.B. A Novel Wave-Absorbing Support System for Mitigating Rock Burst in Deep-Buried Hard Rock Tunnels. *Rock Mech. Rock Eng.* **2026**, 1–21. [CrossRef]
9. Gong, F.; Xu, L.; Dang, W. True-triaxial laboratory tests with relevance to working-face rockburst in deep level bored tunnels. *Eng. Geol.* **2026**, *369*, 108784. [CrossRef]
10. Zheng, L.; Liang, P.; Wang, J. A new method for predicting rockburst intensity levels under unbalanced sample data by integrating deep learning and ensemble learning. *Eng. Anal. Bound. Elem.* **2026**, *189*, 106801. [CrossRef]
11. Li, X.L.; Chen, S.J.; Li, Z.H.; Wang, E.Y. Rockburst mechanism in coal rock with structural surface and the microseismic (MS) and electromagnetic radiation (EMR) response. *Eng. Fail. Anal.* **2021**, *124*, 105396. [CrossRef]
12. Li, X.L.; Wang, E.Y.; Li, Z.H. Rock burst monitoring by integrated microseismic and electromagnetic radiation methods. *Rock Mech. Rock Eng.* **2016**, *49*, 4393–4406. [CrossRef]
13. Miao, D.; Wang, W.; Liu, L.; Yao , K.; Sui, X. Coal mine roof accident causation modeling and system reliability research based on directed weighted network. *Process Saf. Environ. Protect.* **2024**, *183*, 653–664. [CrossRef]
14. Gu, Q.; Cao, A.; Zhao, W. Application of Long-Distance Drilling and Blasting Technology to Prevent Rock Bursts in High-Level Roofs. *Appl. Sci.* **2025**, *15*, 1821. [CrossRef]
15. Ren, H.; Pan, Y.; Luo, H. Analytical Solutions for Energy and Stress Criteria of Coalbursts in Hard-Roof Coal Mining Faces. *Rock Mech. Rock Eng.* **2025**, *58*, 12679–12694. [CrossRef]
16. Zhou, G.; Guo, H.; Sun, H. Advancing support dust evolution mechanism in fully mechanized coal mining face and three-dimensional spraying shield synergistic dust control-removal technology. *Process Saf. Environ. Prot.* **2026**, *209*, 108594. [CrossRef]
17. Turysheva, A.; Kozhubaev, Y.; Changwen, Y. Integrated Control Technologies for Mechanized Coal Mining. *Symmetry* **2025**, *17*, 1947. [CrossRef]
18. Stacey, T.R. The link between the design process in rock engineering and the code of practice to combat rock fall and rockburst accidents. *J. S. Afr. Inst. Min. Metall.* **2004**, *104*, 29–33.
19. Li, W.P.; Lin, B.; Duan, R.J. Inverse determination of ground stress and failure characteristics of surrounding rock in deeply buried tunnel rockburst sections. *Tunn. Undergr. Eng. Disaster Prev.* **2026**, *8*, 59–72. [CrossRef]

20. Zhang, X.B. Optimization of roof support parameters for coal roadways based on suspension theory. *Inn. Mong. Coal Econ.* **2016**, *16*, 131–133.
21. Wei, H. Analysis of the impact manifestation mechanism and energy evolution characteristics in different coal-rock systems. *Saf. Coal Mine* **2020**, *51*, 197–202.
22. Guo, G. Application and Design of Blasting Pre-fracturing, Caving, and Pressure Relief Technology at Xuehugou Mine. *Rock Drill. Mach. Pneum. Tools* **2025**, *51*, 132–134.
23. Li, Y.D.; Li, L.M.; Wang, S. Research process and hotspot prediction of deep-hole presplitting blasting technology in China's mines. *Geomech. Geophys. Geo-Energy Geo-Resour.* **2025**, *11*, 117. [CrossRef]
24. Gubaidullin, R.M.; Davletbaev, Y.A.; Kuzin, G.I. Study of Injection Pressure Differences during the Spontaneous Propagation of Hydraulic Fractures. *J. Appl. Mech. Tech. Phys.* **2026**, *66*, 1041–1051.
25. Cao, L.; Li, J.; Chen, Z. A local parallel FEM for super-hydrophobic proppants in a hydraulic fracturing system based on a 2D/3D transient triple-porosity Navier–Stokes model. *Comput. Math. Appl.* **2026**, *211*, 122–149. [CrossRef]
26. Zhang, B.N.; Hu, W. Analysis and Handling of the Top Cast Material Collapse Accident in the DFH35-1.27-A Boiler Material Separator. *Energy Conserv.* **2016**, *35*, 79–80.
27. Guo, T.; Hu, Z.; Chen, M. Theories, technologies, and future prospects of distributed fiber-optic strain monitoring for hydraulic fracturing. *Int. J. Coal Sci. Technol.* **2026**, *13*, 39. [CrossRef]
28. Li, X.L.; Chen, S.J.; Liu, S.M.; Li, Z.H. AE waveform characteristics of rock mass under uniaxial loading based on Hilbert-Huang transform. *J. Cent. South Univ.* **2021**, *28*, 1843–1856. [CrossRef]
29. Li, H.T.; Li, X.L.; Fu, J.H. Experimental study on compressive behavior and failure characteristics of imitation steel fiber concrete under uniaxial load imitation steel fiber concrete under uniaxial load. *Constr. Build. Mater.* **2023**, *399*, 132599. [CrossRef]
30. Zezekalo, I.; Podoliak, M.; Lartseva, I. Assessment of the technological efficiency and possibility of in-situ regeneration of a heterogeneous catalyst in the composition of proppant for hydraulic fracture of oil formations. *Technol. Audit Prod. Reserv.* **2026**, *2*, 14–20. [CrossRef]
31. Wang, J.W. Gas permeability enhancement and hydraulic fracturing technology for low-permeability coal seams. *Inn. Mong. Coal Econ.* **2026**, *2*, 26–28. [CrossRef]
32. Zhang, Z.; Qiao, J.; Yang, S. A study on the technology of enhancing gas permeability and gas drainage by sectional hydraulic fracturing in directional long boreholes: A case study of the no. 8 coal seam in baode coal mine. *Front. Earth Sci.* **2025**, *13*, 1610921. [CrossRef]
33. Kang, H.P.; Lv, H.W.; Gao, F.Q.; Meng, X.; Feng, Y. Understanding mechanisms of destressing mining-induced stresses using hydraulicfracturing. *Int. J. Coal Geol.* **2018**, *196*, 19–28. [CrossRef]
34. Chang, Q.; Yao, X.; Wang, X.; Yang, S.; Sun, Y. Investigation on hydraulic fracturing and cutting roof pressure relief technology for underground mines: A case study. *Lithosphere* **2021**, *2021*, 4277645. [CrossRef]
35. Liu, P.; He, Y.; Zhu, R. Numerical analysis of hydraulic fracturing behavior in layered shale reservoirs considering the coupling effects of conductivity and shear strength of multiple bedding planes. *Eng. Fract. Mech.* **2026**, *340*, 112152. [CrossRef]
36. Liu, B.; Xu, T.; Meredith, G.P. A coupled stress-permeability model for hydraulic fracturing in layered shale: Insights into damage and permeability evolution. *J. Cent. South Univ.* **2026**, 1–27. [CrossRef]
37. Wang, X.; Feng, Y.; Zhang, F. Investigation on breakage and collapse characteristics of hard and thick roof during coal excavation subject to hydraulic fracturing. *Eng. Fail. Anal.* **2025**, *181*, 109935. [CrossRef]
38. Zoback, D.M.; Singh, A. Development of continuous estimates of the least principal stress with depth for application to multi-stage hydraulic fracturing. *Geomech. Geophys. Geo-Energy Geo-Resour.* **2026**, *12*, 49. [CrossRef]
39. Liu, S.M.; Sun, H.T.; Zhang, D.M. Experimental study of effect of liquid nitrogen cold soaking on coal pore structure and fractal characteristics. *Energy* **2023**, *275*, 127470. [CrossRef]
40. Nguyen, T.H.; Ganat, A.A.T.; Truong, V.T. Maximizing oil production efficiency in mature field: A strategic approach to optimizing recovery and extending field life. *Pet. Sci. Technol.* **2026**, *44*, 1313–1328.
41. Kurlenya, V.M.; Rybalkin, A.L.; Serdyuk, M.I. Physical Modeling of Hydraulic Fracturing in Rock Mass with Conductive Fractures and a Cavity. *J. Min. Sci.* **2026**, *61*, 747–756.
42. Xiao, H.; He, T.; Wang, H. Competitive Propagation Laws of Hydraulic Fractures in Multiple Thin Coal Seams. *ACS Omega* **2026**, *11*, 24346–24360. [CrossRef] [PubMed]
43. Gu, H.; Ma, F. Simulation of acid fracturing using a thermal-hydraulic-mechanical-chemical coupling model integrating fracture initiation and propagation. *Geomech. Energy Environ.* **2026**, *46*, 100830. [CrossRef]
44. Safarpour Kapoorchali, Z.; Kazemzadeh, E.; Arian, M.; Kianoush, P. Quantification of fracture porosity and reservoir heterogeneity in carbonates: An integrated core-log zoning workflow, Southwest Iran. *Results Earth Sci.* **2026**, *4*, 100149. [CrossRef]

Disclaimer/Publisher's Note: The statements, opinions and data contained in all publications are solely those of the individual author(s) and contributor(s) and not of MDPI and/or the editor(s). MDPI and/or the editor(s) disclaim responsibility for any injury to people or property resulting from any ideas, methods, instructions or products referred to in the content.